Optimizing pump-probe reflectivity measurements of ultrafast photoacoustics with modulated asynchronous optical sampling

M. C. Velsink,[1, a)] M. Illienko,[1] P. Sudera,[1] and S. Witte[1, 2, b)]
[1)]*Advanced Research Center for Nanolithography (ARCNL), Science Park 106, 1098 XG Amsterdam, The Netherlands*
[2)]*Department of Physics and Astronomy, Vrije Universiteit, De Boelelaan 1081, 1081 HV Amsterdam, The Netherlands*

(Dated: 23 August 2023)

Time-resolved optical pump-probe experiments enable the study of complex light-matter interactions on ultrafast timescales, provided that they reach sufficient sensitivity. For instance, with pump-induced ultrafast photoacoustics, probing the typically small changes in optical properties requires a high signal-to-noise ratio. Asynchronous optical sampling (ASOPS), using two separate pulsed lasers at slightly different repetition rates, can be effective at removing noise by averaging many rapidly acquired traces. However, the pump-probe delay scan with ASOPS is always as long as the pump pulse interval, which is inefficient if the delay-time range of interest is shorter. Here, we demonstrate two modified ASOPS schemes that optimize the measurement efficiency by only scanning the range of interest. The modification based on frequency modulated ASOPS (MASOPS) is most efficient, especially in the presence of low-frequency flicker noise. We provide a proof-of-concept measurement of ultrafast photoacoustics in which we use MASOPS to scan a time delay of $1/20$ of the pump pulse interval. The resulting noise floor is $\sqrt{20}$ times lower compared to conventional ASOPS, allowing for 20 times faster measurements. Furthermore, we show that by taking experimental noise characteristics into account, more traditional pump-probe methods can also be optimized.

I. INTRODUCTION

Many materials display complex dynamics on ultrashort timescales, originating from interactions involving electrons, phonons, thermal transport, and more. Ultrafast laser pulses provide a means to capture such transient phenomena, often through time-resolved optical spectroscopy. In such pump-probe methods, the dynamics are both optically initiated and detected through some form of light-matter interaction.[1]

For instance, ultrafast laser pulses can be used to generate high-frequency acoustics in absorbing materials. These pump-induced strain pulses can subsequently be optically detected as they modulate the optical properties of the material.[2,3] This type of light-matter interaction has diverse applications, from studying surface acoustic waves[4,5] and other fundamental phononic phenomena[6–8] to characterizing and imaging biological cells.[9,10] Ultrafast photoacoustics can also be used to "look through" opaque thin layers, by both exciting an acoustic pulse and detecting its echo optically at the top surface.[11,12] This concept can be further extended to the detection of buried diffraction-based markers in semiconductor device manufacturing.[13] Typically, the acoustically induced changes in optical properties are weak, with reflectivity changes of only 10^{-7} to 10^{-3}. This makes low-noise pump-probe measurements a necessity. Reducing noise also allows for faster acquisition, which is especially desirable for minimizing pixel dwell time in spatially resolved measurements.

In general, the frequency content of ultrafast pump-induced phenomena can span hundreds of gigahertz, which makes real-time probing challenging. Instead, in a typical pump-probe experiment the pump-induced effects are probed at slowly increasing delay times. This adjustable delay can be achieved with fs-to-ps resolution by splitting a single pulse into pump and probe paths and recombining them after a mechanically adjustable delay line, or by using asynchronous optical sampling (ASOPS) with two separate lasers.[14] Measuring the probe reflectivity over time then gives an equivalent-time representation of the actual reflectivity signal, with greatly reduced frequency content. Because the delay in ASOPS is purely time-based, it does not suffer from beam pointing variation and divergence changes, as is the case with a mechanical delay line. However, the total measured delay is always equal to the pump pulse interval, which is inefficient if the delay-time range of interest is shorter.

In this paper, we present an ASOPS-based experimental apparatus for ultrafast pump-probe reflectivity measurements, capable of reaching shot-noise-limited detection sensitivity. With this setup, we implement two modified ASOPS scanning methods that circumvent the delay-scan inefficiency of conventional ASOPS. We demonstrate that with our setup for measuring ultrafast photoacoustics, adding frequency modulation to ASOPS improves noise by more than an order of magnitude. With further analysis, we motivate that by taking into account the noise characteristics of an experiment, mechanical pump-probe setups can also be optimized.

A. Asynchronous optical sampling

The concept of ASOPS is schematically depicted in Fig. 1. Each pump pulse induces the same reflectivity change in the sample, which is detected by a probe pulse. Because the pump repeats slightly faster than the probe, the delay between probe and pump slowly increases. In this way, the fast reflectivity dynamics are sampled at a different delay for each next probe pulse. With a nominal repetition rate f_0 and an offset Δf,

[a)]Electronic mail: m.velsink@arcnl.nl
[b)]Electronic mail: s.witte@arcnl.nl

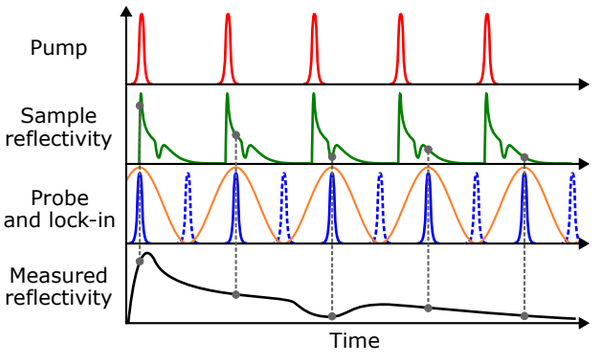

FIG. 1. Schematic depiction of ASOPS. The pump repeats slightly faster than half the probe repetition rate, causing an increasing pump-probe delay. Measuring the probe intensity then recovers the ultrafast dynamics in the sample reflectivity. The dashed probe pulses are not affected by the pump but are used for noise reduction with lock-in detection, as explained in the setup description.

every probe pulse arrives $\Delta t \approx \Delta f / f_0^2$ later, giving an effective delay scan speed of $\nu = f_0 \cdot \Delta t \approx \Delta f / f_0$. The delay scan speed of ASOPS typically far exceeds that of mechanical delay lines. For example, scan speeds of 400 ns/s and higher are readily achievable, which would require a mechanical stage moving at 60 m/s for a single-reflection delay line.

Usually, the pump and probe in ASOPS run at similar repetition rates. Instead, in our setup the pump runs at approximately half the probe repetition rate. This allows us to use lock-in detection at half the probe repetition rate, as indicated in Fig. 1, which reduces electronic noise.

B. Modified scanning methods

In conventional ASOPS, the repetition rate offset of the pump is fixed, and many rapidly-acquired traces are averaged together. As mentioned before, this has the disadvantage that the resulting trace is as long as the pump pulse interval, making measurements of a short range in time inefficient. High-speed ASOPS systems with increased repetition rates of 1 GHz to 10 GHz can already improve this inefficiency,[15–21] but such systems do not have the flexibility of measuring longer delay times as well. Instead, by modulating the repetition rate offset in time, the pump-probe delay can be alternated back and forth over the range of interest. Such a modified scanning scheme enables much greater data collection efficiency. A similar approach has been explored before in terahertz radiation experiments.[22–24] However, our approach does not require delay time calibration and is easy to apply to ASOPS systems with a tunable repetition rate. An alternative efficient solution with synchronized lasers is to measure at a small repetition rate offset, slowly scanning the range of interest only once but with increased integration time per unit delay. This is similar to using a mechanical delay stage in a traditional pump-probe setup. We will thus compare these three methods:

1. Modulated ASOPS (MASOPS),
2. Conventional ASOPS,
3. Single slow scan.

C. Signal and noise theory

To understand the signal-to-noise ratio resulting from each scan method, a detailed analysis is instructive. We consider a signal that contains an additive noise source $\delta_a(t)$ with mean 0, and a multiplicative noise source $\delta_m(t)$ with mean 1. The resulting measured signal for the i^{th} trace in a (M)ASOPS measurement is then given by

$$M_i(t') = \delta_m(t_i + t') \cdot S(\Delta t(t')) + \delta_a(t_i + t'), \qquad (1)$$

where $S(\Delta t(t'))$ is the true signal at pump-probe delay Δt, t_i the trace start time (with $t_1 = 0$), and $t' = t - t_i$. Since the scan speed ν is the ratio between delay time and real time, $S(\Delta t(t')) = S(\nu t')$. After collecting N traces, the average measurement signal is given by

$$M(t') = \frac{1}{N} \sum_{i=1}^{N} \left[\delta_m(t_i + t') \cdot S(\nu t') + \delta_a(t_i + t') \right]. \qquad (2)$$

The signal for the slow scan method has the same form, with $N = 1$.

With a pump pulse interval τ, we are interested in a short delay-time range $\alpha\tau$ with $\alpha \leq 1$. Then, combined with a rapid scan rate of λ traces/s for (M)ASOPS, and an integration time T, we can find the scan speed ν for the three methods. The slow scan method uses $\nu = \alpha\tau/T$, ASOPS uses $\nu = \lambda\tau$, and MASOPS uses $\nu = \lambda\alpha\tau$. For a desired equivalent measurement bandwidth $f_{\text{BW}}^{\text{eq}}$, which is equal for all methods, the required lock-in filter bandwidth f_{L} is given by $f_{\text{L}} = \nu \cdot f_{\text{BW}}^{\text{eq}}$.

If the combined noise within f_{L} is predominantly white, the root-mean-square (RMS) noise scales with $\sqrt{f_{\text{L}}}$. After averaging, this is reduced by $\sqrt{N}$, as each trace samples uncorrelated noise. Even though MASOPS uses an f_{L} that is a factor $\nu_{\text{MASOPS}}/\nu_{\text{slow}} = \lambda T$ higher than the slow scan method, after averaging $N = \lambda T$ traces the noise will be the same. However, ASOPS will have $\sqrt{1/\alpha}$ times more noise.

Apart from white noise, flicker noise with a $1/f$ power spectral density can be significant at low frequencies.[25] There is then some corner frequency f_{c} below which flicker noise dominates. With lock-in detection, additive flicker noise can be avoided by demodulating at a frequency well above f_{c}. The additive noise in our experiment is therefore expected to be white.

However, multiplicative flicker noise cannot be removed using lock-in detection, as it appears as amplitude modulation around the demodulation frequency. Combined with a non-zero signal, this multiplicative noise can have a higher contribution than additive noise up to f_{c}. But as long as f_{L} is greater than f_{c}, additive noise will still dominate and multiplicative noise will not play a role in the measured signal. Moreover, for (M)ASOPS, if $\lambda \geq f_{\text{c}}$, the multiplicative noise $\delta_m(t_i + t')$ can be assumed constant for $0 \leq t' \leq 1/\lambda$. In that

case,

$$M(t') \approx S(\nu t') \cdot \frac{1}{N}\sum_{i=1}^{N} \delta_m(t_i) + \frac{1}{N}\sum_{i=1}^{N} \delta_a(t_i + t'), \qquad (3)$$

so that the signal shape is not changed by multiplicative noise, but only scaled by the average of δ_m.

For the slow scan method, f_L is typically much lower than for (M)ASOPS, and can become comparable or lower than f_c. In that case, flicker noise dominates. The integrated RMS noise between equivalent frequencies f_1^eq and f_2^eq, or real-time frequencies $f_{1,2} = \nu \cdot f_{1,2}^\mathrm{eq} = \alpha\tau \cdot f_{1,2}^\mathrm{eq}/T$, is then given by

$$\mathrm{RMS}_\mathrm{noise} \propto \sqrt{\int_{f_1}^{f_2} 1/f \,\mathrm{d}f} = \sqrt{\ln\left(\frac{f_2}{f_1}\right)} = \sqrt{\ln\left(\frac{f_2^\mathrm{eq}}{f_1^\mathrm{eq}}\right)}, \quad (4)$$

which is completely independent of T. So, integrating longer with reduced f_L will not help to remove this noise. Averaging more traces will still help, as the slow scan method then starts to work like MASOPS.[26]

In general, the characteristics of noise and whether $1/f$ noise plays a role depends on the pump-probe experiment. Without lock-in detection, additive flicker noise might be dominant. Furthermore, higher noise at lower frequencies does not necessarily follow a $1/f$ trend. However, the (M)ASOPS methods will still have the advantage of higher frequency content due to their high ν compared to the slow scan method. This means low frequency noise has less effect on the measured signal shape. In our experiments, we measure laser-induced ultrafast photoacoustics and can compare and verify the performance of the three methods directly, based on their noise floor.

II. EXPERIMENTAL SETUP

The setup for measuring laser-induced ultrafast photoacoustics is sketched in Fig. 2. The pump laser is a 1030 nm ytterbium fiber laser with 180 fs pulse duration at 50 MHz (Menlo Systems Orange). It is electronically synchronized to the free-running probe laser, an erbium fiber laser with 70 fs pulse duration at 100 MHz, from which we use the 780 nm second-harmonic output (Menlo Systems C-Fiber 780). The pump and probe are collinearly focused onto the sample. In the following, we use a 400 nm thin freestanding aluminum membrane as the test sample to characterize the measurement system performance. To generate and detect photoacoustic signals in this sample, we use 75 mW pump power and 2 mW probe power. A beam expander in the probe path ensures the probe spot is smaller than the pump on the sample ($\sim$4 µm versus $\sim$8 µm, respectively).

Half of the reflected probe light is then detected in one port of a multimode fiber-coupled balanced detector, with a reference probe beam in the other port. An OD6 low-pass dichroic filter in the probe arm prevents any pump light from being detected. The fast balanced detector (500 MHz, Femto HBPR) has 5 kV/A transimpedance gain, allowing for shot-noise-limited probe detection at mW-level intensities. Additionally, a lock-in amplifier (Zurich Instruments UHFLI) filters and amplifies the detector signal at half the probe rate. The lock-in output can either be saved directly or captured by an oscilloscope for trace averaging in case of (M)ASOPS. Because the balanced detector also outputs a DC voltage, we can extract the relative reflectivity change as $\Delta R/R_0 = \sqrt{2} \cdot V_\mathrm{RMS}/V_\mathrm{DC}$ (see Appendix A). Here, V_RMS is the RMS voltage as measured by the lock-in amplifier, V_DC the DC voltage, ΔR the absolute reflectivity change, and R_0 the reflectivity without pump. We assume that any pump-induced effects have vanished before the secondary probe pulses (dashed in Fig. 1) are reflected.

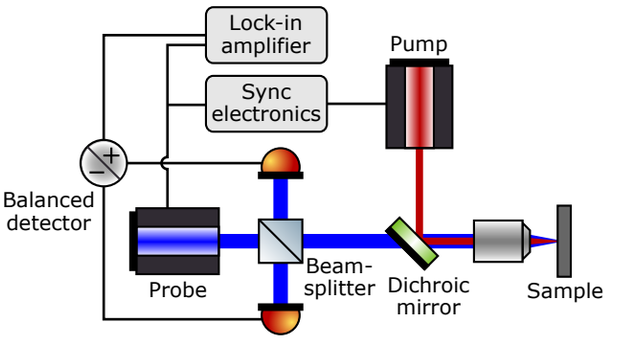

FIG. 2. Sketch of the measurement setup. The pump and probe are collinearly focused onto the sample. Half of the reflected probe light is coupled into a multimode fiber and detected by a fast detector, which is balanced with a reference probe beam. The detector signal is then filtered and amplified at half the probe rate.

A. Synchronization and modulation electronics

The control electronics are shown schematically in Fig. 3. The pump and probe pulses are internally detected with fast photodiodes and their repetition rate harmonics at 1 GHz are electronically band-pass filtered. A 20 MHz reference is subtracted from the probe's 1 GHz, after which the resulting 980 MHz is compared to the pump's 1 GHz, creating a 20 MHz intermediate frequency. This frequency is phase-locked via a PID loop to a digitally generated 20 MHz signal, which can be frequency and/or phase modulated to provide a modulated pump repetition rate. The PID loop with 100 kHz bandwidth controls the pump laser by an intracavity mirror that can be moved in large steps by a stepper motor and fine-tuned with a piezo element. Detecting pump and probe phases at 1 GHz increases sensitivity, as any phase fluctuations in the fundamentals are multiplied by the harmonic number (20 for the pump and 10 for the probe, respectively). Furthermore, the effect of phase noise in the 20 MHz reference is reduced by a factor 10 as well, compared to phase detection at 100 MHz. The complete synchronization setup is a commercial system (Menlo Systems RRE-SYNCRO), with a jitter of 59 fs as measured by Menlo Systems. In practice, the time resolution is

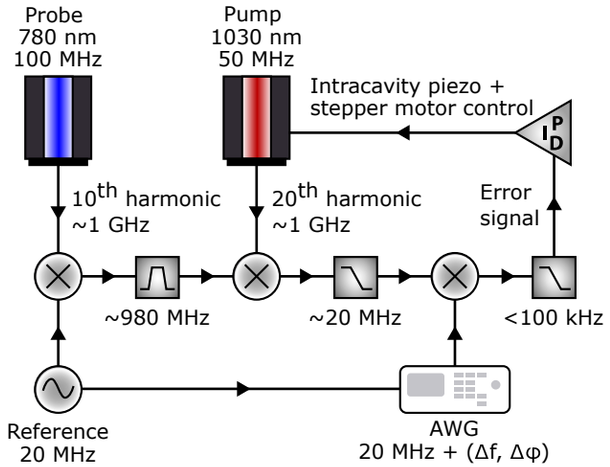

FIG. 3. Block diagram of the MASOPS synchronization electronics. The pump and probe repetition rates are compared by their 1 GHz electronic harmonics, at a 20 MHz offset. The resulting intermediate frequency is locked to the signal from an arbitrary waveform generator (AWG), via a PID-loop that controls an intracavity mirror in the pump laser. Any desired modulation can be added with the AWG.

limited by the 180 fs pump pulse duration, which we have verified with a pump-probe intensity cross-correlation on a two-photon GaP photodetector.

We have added an arbitrary waveform generator (AWG, Keysight 33522B) to allow for modulation of the frequency and phase offset. A frequency shift Δf or phase shift $\Delta\varphi$ of the AWG output will result in a repetition rate offset of $\Delta f/20$ or shift of $\Delta\varphi/20$, respectively. Previously, modulation has been applied as a voltage offset to the PID loop, which requires accurate voltage-to-phase calibration[22] or a known repetitive signal.[23] Instead, in our approach the modulation is essentially directly applied to the 1 GHz harmonic of the pump, giving a quantitative and calibration-free conversion to the resulting time delay scan. For example, a 1 Hz offset of the AWG results in a delay scan speed of 1 ns/s. Due to AC voltage limitations of the intracavity piezo element in the pump laser, the scan speed modulation is limited from -20 ns/s to $+20$ ns/s. Alternating traces of 1 ns long can thus be measured at a maximum rate of 20 traces per second.

B. Settings for scanning methods

With modulated ASOPS in our experiment, the pump runs at $+1$ Hz offset for $1/20$ s and then -1 Hz offset for $1/20$ s, resulting in 20 traces per second of 1 ns long with alternating direction. The modulation is applied via phase modulation, as frequency modulation otherwise results in a slight timing drift after every cycle with our AWG. A triangle wave defines the modulation waveform, with the transitions smoothened in order to prevent sharp PID input jumps. The majority of the waveform (90 %) remains linear, and the known nonlinearity in the transitions is corrected for in the data analysis. See Appendix B for more details. On average, the scan speed ν is 20 ns/s. With conventional ASOPS, the pump runs at a fixed $+20$ Hz offset, resulting in 20 traces per second of 20 ns long ($\nu = 400$ ns/s). Additionally, we can do a single slow scan in T seconds by running the pump at $+1/20T$ Hz, resulting in a trace of 1 ns long ($\nu = 1/T$ ns/s).

The lock-in amplifier uses a fourth-order cascaded digital low-pass filter, with its bandwidth set such that the equivalent measurement bandwidth is always 1 THz. Thus, it is set to 20 kHz for MASOPS, 400 kHz for ASOPS, and $1000/T$ Hz for the slow single scan. The sample rate of the data acquisition is approximately ten times higher to minimize aliasing.

We compare the three methods at different integration times. For (M)ASOPS, the integration time is increased by averaging more traces, but the scan speed and lock-in settings remain fixed. However, for the slow single scan, the scan speed and lock-in filter bandwidth are adjusted for each integration time T.

III. RESULTS AND DISCUSSION

The change in reflectivity of the sample over time due to pump-induced effects is plotted in Fig. 4. Initially, the pump pulse rapidly heats up the electrons in the metal, causing a large and rapid reflectivity increase. The electrons subsequently transfer their thermal energy to the lattice through electron-phonon coupling, after which an acoustic pulse is generated by thermal expansion. This pulse travels through the freestanding aluminum membrane and reflects back-and-forth many times. The resulting echoes can be detected due to the photoelastic effect, with the first one arriving after 123 ps. Acoustic damping decreases the amplitude of subsequent echoes, but they are still clearly visible after 1000 ps. Most signal features, such as the initial electronic peak, shape of the acoustic pulse, and magnitude of the reflectivity change, strongly depend on the sample and experimental configuration. These effects have been studied before,[27,28] and are not the focus of this work.

The inset of Fig. 4 shows a visual comparison of the three methods around the fifth echo, measured with an integration time of 20 s. It is clear that the MASOPS and slow scan traces are significantly less noisy than the ASOPS trace. In addition, there are small oscillations present in the slow scan trace that are absent in the MASOPS trace. We have also observed that the slow single scan can have slight timing drifts up to ± 2 ps on a timescale of 1000 s, which are likely caused by low frequency drift in the synchronization hardware. However, even a mechanical delay stage with a low resolution of 0.05 mm will have an order of magnitude better timing accuracy. The timing drift we observe is therefore mostly specific to our setup. The low frequency drifts are not relevant for the (M)ASOPS methods, as they occur on a timescale that is longer than the time needed to measure a single trace.

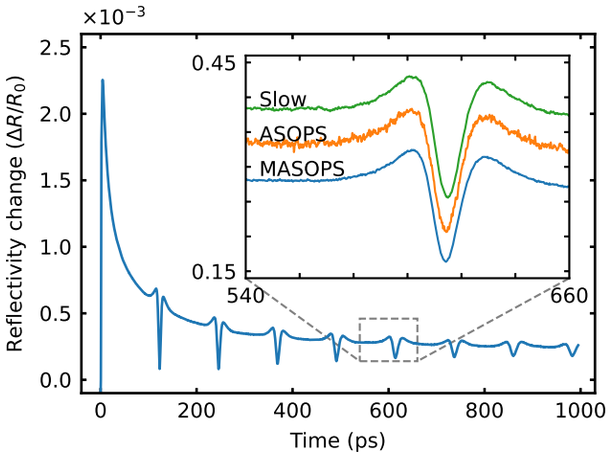

FIG. 4. Pump-induced relative reflectivity change in the aluminum membrane over time. The inset shows the fifth acoustic echo in more detail, measured with the three methods at 20 s integration time. Each trace is offset by 0.05×10^{-3} for clarity. MASOPS appears less noisy than ASOPS, and does not have the small oscillations as present in the slow single trace.

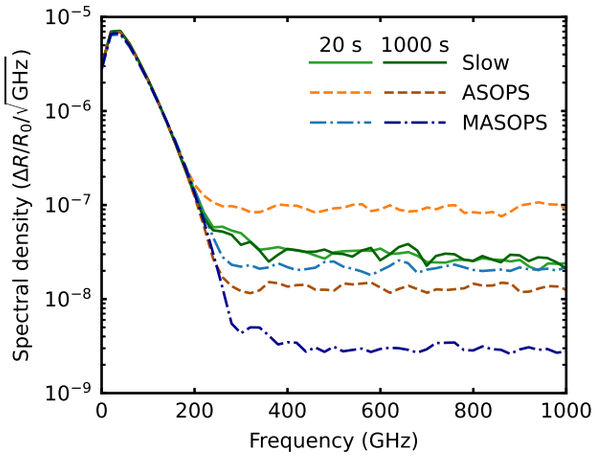

FIG. 5. Spectral density estimates of the measured traces with the three different methods, corrected for the lock-in filter response. The light colored lines are for 20 s integration time, and the darker lines for 1000 s. There is signal content present up to 300 GHz, above which noise dominates. Even though the integration time increases 50-fold, the noise floor of the slow single scan does not improve.

A. Spectral noise density comparison

In order to quantitatively compare the three measurement schemes, we estimate their spectral noise density by using Welch's method.[29] The method works by taking partially overlapping Fourier transforms of small segments of the data and averaging the Fourier amplitudes for each frequency bin. This reduces amplitude variations at the cost of frequency resolution, allowing for accurate spectral density estimation. We apply Welch's method from 40 ps to 970 ps, using 36 Hann-windowed segments of 50 ps long with optimal 50 % overlap.[30]

The resulting spectral density estimates are shown in Fig. 5 for 20 s and 1000 s integration time. There is signal content present up to 300 GHz, which has equal amplitude for all methods until noise starts to dominate. However, the noise floors vary significantly. For the shorter integration time, MASOPS has the lowest noise floor, followed by the slow single scan, and then by ASOPS. In our case, this difference is mostly relevant for high-frequency signal content above 200 GHz. However, with weaker signal, the noise floor improvement should already become apparent at lower frequencies. With 50 times longer integration, both the MASOPS and ASOPS noise floors decrease by a similar ratio close to $\sqrt{50}$. In contrast, the slow single scan does not improve at all.

The improvement with longer integration times is easier to see by averaging the spectral density from 400 GHz to 1000 GHz, as shown in Fig. 6. Both MASOPS and ASOPS follow the same $1/\sqrt{T}$ trend, as expected. However, MASOPS has approximately $\sqrt{20}$ times less noise than ASOPS due to the much-improved measurement efficiency in the short time range of interest. It is possible to achieve the same noise level with conventional ASOPS, but it will take 20 times longer. As the slow single scan also only measures the time range of interest, it should have similar efficiency to MASOPS. For short integration times, the slow single scan indeed follows the noise floor of MASOPS. Nevertheless, the slow scan noise floor stagnates beyond 20 s, as was already apparent from Fig. 5. This suggests that the slow single scan is sensitive to a different kind of noise that cannot be removed by measuring slower and reducing the lock-in filter bandwidth further.

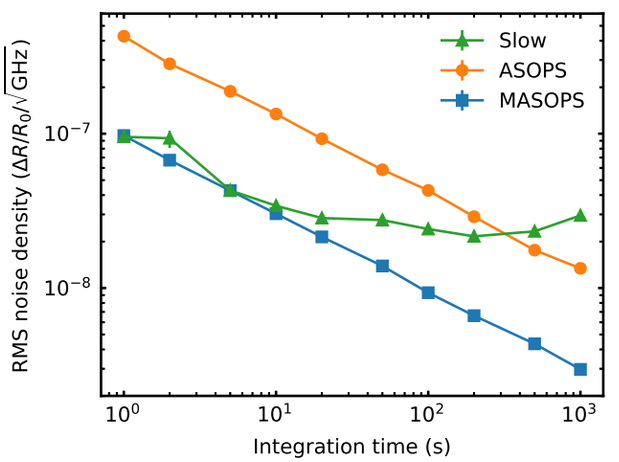

FIG. 6. Root-mean-square (RMS) noise density from 400 GHz to 1000 GHz for different integration times. The error bars (typically smaller than the symbols) indicate the 95 % confidence interval based on the variance within the frequency range. MASOPS has $\sqrt{20}$ times less noise than ASOPS, but both methods improve with $1/\sqrt{T}$. Although the slow single scan method is comparable to MASOPS for short integration times, it reaches a plateau after 20 s.

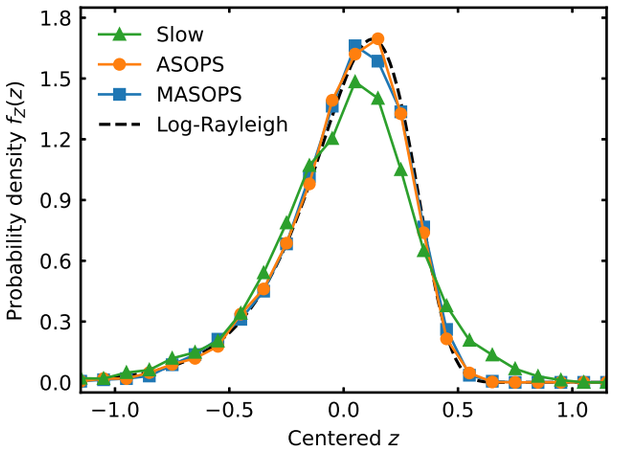

FIG. 7. Probability density of $z = \log_{10}(A_{\text{noise}})$ for the noise density A_{noise} from 400 GHz to 1000 GHz, averaged over all integration times of 50 s and longer. For each method, z is centered by subtracting the mean of z. The black dashed line indicates the theoretical Log-Rayleigh distribution for uncorrelated Gaussian noise. Only the slow single scan deviates significantly, with high-valued outliers.

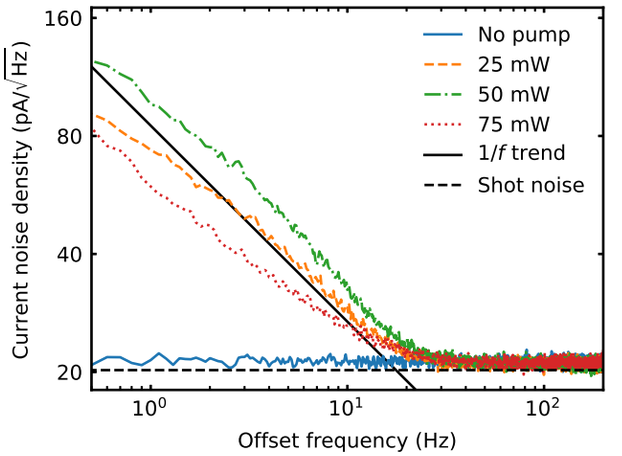

FIG. 8. Spectral noise density of the balanced photocurrent for a one-hour measurement using different pump powers, with the pump-probe delay fixed at 300 ps. A $1/f$ trend and the shot noise level are indicated in black. Without pump, shot noise dominates and $1/f$ noise is absent. The $1/f$ noise is similar for different pump powers.

B. Noise characterization

We can characterize the noise by the probability distribution of noise amplitudes A_{noise} of the Fourier transform. For uncorrelated Gaussian white noise, A_{noise} should follow the Rayleigh distribution. To better compare the shape of the distribution for both low and high values, we look at the distribution of $z = \log_{10}(A_{\text{noise}})$. This has the advantage that normalization by the mean is a shift in z, which preserves the shape of the histogram.[31] The probability density function of the resulting Log-Rayleigh distribution with zero mean is given by

$$f_Z(z) = \ln(10) 10^{2(z-\overline{z})} \exp\left(-10^{2(z-\overline{z})}/2\right), \qquad (5)$$

where $\overline{z} = \frac{1}{2}(\ln(2) - \gamma)/\ln(10)$, with γ Euler's constant. See Appendix C for the derivation of Eq. 5.

We estimate the probability density shape of $\log_{10}(A_{\text{noise}})$ between 400 GHz and 1000 GHz by taking a histogram for each frequency bin in the Fourier transforms from Welch's method. Then, we center each histogram by subtracting the mean and calculate the average histogram over all frequency bins. To compare the methods in the range where the slow scan method deviates, we average the resulting histograms for each integration time of 50 s and longer. These final histograms for each method are shown in Fig. 7, together with Eq. 5. The (M)ASOPS methods fit the Log-Rayleigh shape well. However, the slow single scan significantly deviates, with high-valued outliers. This indicates that (M)ASOPS averages white, uncorrelated Gaussian noise, whereas the slow single scan does not.

C. Low frequency 1/f noise

To further investigate the type of noise, we fix the pump-probe delay at 300 ps and record the lock-in amplified balanced detector signal for one hour. Again, we estimate the spectral noise density with Welch's method using Hann-windowed segments of 10 s long. For 2 mW probe power, the photocurrent in each photodiode from the balanced detector is approximately 320 µA. The shot noise for both current paths adds in quadrature, increasing its total value by $\sqrt{2}$. Furthermore, because the shot noise is pulsed and in phase with the lock-in demodulation, the resulting shot noise again increases by $\sqrt{2}$.[32] The resulting shot noise current density is thus $20.3\,\text{pA}/\sqrt{\text{Hz}}$. The noise density for different pump powers is plotted in Fig. 8. Without pump, shot noise dominates. With pump, low frequency noise appears that follows a $1/f$ trend in squared density. In our experience, the exact slope and magnitude of this $1/f$-like noise can change with alignment and pump power, but the $1/f$ corner is consistently around 20 Hz.

With a lock-in bandwidth of 20 kHz and 400 kHz for MASOPS and ASOPS, respectively, their noise floors are dominated by white (shot) noise. However, the slow single scan method has a lock-in bandwidth of $1000/T$ Hz, which becomes smaller than the $1/f$ corner around 50 s integration time. In that case, the $1/f$ flicker noise starts to dominate. As shown before in Eq. 4, the average noise will then be completely independent of T. For any pump-probe setup that uses a slow scan method, it is therefore valuable to find out if there is significant $1/f$ noise present and what its corner frequency is. Using an acquisition time with a corresponding lock-in bandwidth that approaches this corner frequency is then the optimal configuration. If a lower noise floor is required, only trace averaging will help, which is the approach taken with (M)ASOPS.

IV. CONCLUSION

We have shown that applying frequency modulation to ASOPS greatly increases measurement efficiency if the delay-time range of interest is short compared to the pump pulse interval. In our example, with a 1 ns range of interest and 20 ns pump pulse interval, MASOPS has $\sqrt{20}$ times less noise, allowing for 20 times faster measurements. This advantage further increases with a shorter range of interest, or with a longer pump pulse interval. With MASOPS and lock-in amplification, we can measure ultrafast photoacoustics at the shot noise limit.

Compared to MASOPS, a slow scanning method can achieve similar noise performance, provided white noise dominates. However, if there is significant $1/f$ flicker noise present, longer integration times cannot improve the noise floor. For pump-probe setups that use slow (mechanical) scanning methods, the noise floor can therefore be optimized by setting the measurement bandwidth to the $1/f$ corner frequency. In that case, further noise reduction is only possible with trace averaging.

ACKNOWLEDGMENTS

We acknowledge support from the European Research Council (ERC-CoG 864016, project 3D-VIEW), the Dutch Research Council NWO (TTW-HTSM 17960, project Orpheus), and the European Union's Horizon 2020 program (ECSEL Joint Undertaking IT2, project 875999).

We thank Irwan Setija (ASML), Stephen Edwards (ASML), and Paul Planken (ARCNL) for fruitful discussions.

DATA AVAILABILITY

The data that support the findings of this study are available from the corresponding author upon reasonable request.

Appendix A: Extracting relative reflectivity

For a fixed pump-probe delay Δt, the probe repeats exactly twice as fast as the pump, as indicated in Fig. 1. In general, the n^{th} probe pulse that reflects from the sample has an intensity $I_n(t) = R(n)E_0\delta(t - n\tau/2)$, with $R(n)$ the reflectivity, E_0 the incident pulse energy, $\delta(t)$ the Dirac delta function, and τ the pump pulse interval. If the detector is linear and has infinite bandwidth, the unbalanced voltage in the sample beam detector is simply $V(t) = S \cdot I(t)$, with S the detector sensitivity including experimental losses. We only need to consider the effect of a single pump pulse on the two following probe pulses, since all signals are periodic with the pump. We assume that any pump-induced reflectivity modulation vanishes quickly, so that the second probe pulse observes the unmodified reflectivity $R(1) = R_0$. The first probe pulse is however modified, and observes $R(0) = R_0 + \Delta R$. With the pump pulse arriving at $t = -\Delta t$, the DC voltage over the two probe pulses until the next pump pulse is given by

$$\begin{aligned} V_{\text{DC}} &= \frac{1}{\tau}\int_{-\Delta t}^{-\Delta t+\tau} V(t)\mathrm{d}t \\ &= \frac{S\cdot E_0}{\tau}\int_{-\Delta t}^{-\Delta t+\tau} [R(0)\delta(t) + R(1)\delta(t-\tau/2)]\,\mathrm{d}t \\ &= \frac{S\cdot E_0}{\tau}\left[2R_0 + \Delta R(\Delta t)\right] \approx 2\cdot R_0\frac{S\cdot E_0}{\tau}, \end{aligned} \tag{A1}$$

where we have assumed $\Delta R \ll R_0$. We always use the unbalanced DC voltage for V_{DC}, as the balanced signal has no DC component. The lock-in amplifier demodulates at half the probe repetition rate and in phase with the probe pulse train, by multiplying the voltage with $\sqrt{2}\cos(2\pi\cdot t/\tau)$ and averaging. The resulting RMS voltage is given by

$$\begin{aligned} V_{\text{RMS}} &= \frac{\sqrt{2}}{\tau}\int_{-\Delta t}^{-\Delta t+\tau} \cos(2\pi\cdot t/\tau)\cdot V(t)\mathrm{d}t \\ &= \frac{\sqrt{2}\cdot S\cdot E_0}{\tau}\left[R(0) - R(1)\right] \\ &= \sqrt{2}\cdot\Delta R(\Delta t)\frac{S\cdot E_0}{\tau}. \end{aligned} \tag{A2}$$

With balancing, V_{RMS} is the same, but laser noise will be reduced. Note that in practice, the detector bandwidth is finite. However, as long as the bandwidth is greater than $1/\tau$, V_{RMS} remains unchanged as the signal at half the probe repetition rate will not be filtered out. Hence, we can reconstruct the relative reflectivity change by $\Delta R/R_0 = \sqrt{2}\cdot V_{\text{RMS}}/V_{\text{DC}}$.

Appendix B: Modulation waveform

The phase modulation waveform we use is effectively a rounded triangular wave. The normalized upswing $\hat{\phi}$ of the waveform is a piecewise continuous function of the normalized time $\hat{t}$, given by

$$\hat{\phi}(\hat{t}) = \begin{cases} (1-p)\dfrac{1-\cos(\omega\hat{t})}{2} & 0 \le \hat{t} \le T \\ \dfrac{1-a}{2} + a\cdot\hat{t} & T < \hat{t} < 1-T \\ 1-\hat{\phi}(1-\hat{t}) & 1-T \le \hat{t} \le 1. \end{cases} \tag{B1}$$

Here, $0 \le p < 1$ parametrizes how much of the total modulation range should be scanned linearly, with derived parameters $\omega = \pi + 2p/(1-p)$, $T = \pi/(2\omega)$, and $a = \omega(1-p)/2$. In our experiments, we typically use $p = 0.9$. Since $\hat{\phi}(0) = 0$ and $\hat{\phi}(1) = 1$, the waveform $\Delta\varphi(t)$ for any arbitrary modulation range or modulation rate can simply be found by scaling $\hat{\phi}$ or $\hat{t}$, respectively. The waveform is then combined with its mirror image to form the final up-down modulation waveform that can be uploaded to the arbitrary waveform generator. As the phase maps directly to a pump-probe delay, in the analysis

the nonlinear cosine part can be interpolated to give a linear time delay axis. The conversion between a phase shift $\Delta\varphi$ and the effective pump-probe delay depends on the synchronization details, but in our case 360° results in 1 ns of delay (see section II A).

Appendix C: Log-Rayleigh distribution

The Log-Rayleigh distribution has the advantage that its shape does not depend on the mean, which helps with noise classification. We follow a similar derivation as in Ref. 31, but use the base 10 logarithm instead of the natural logarithm.

For uncorrelated Gaussian white noise, the real (X) and imaginary (Y) Fourier coefficients are also Gaussian distributed with uniform random phase and equal variance. The amplitude $A = \sqrt{X^2+Y^2}$ then follows a chi-distribution with two degrees of freedom, also known as the Rayleigh distribution. If the standard deviations of X and Y are unity, then the probability density function of A is given by

$$g(A) = Ae^{-A^2/2},\ A \geq 0. \tag{C1}$$

With $z = \log_{10}(A)$, z is strictly increasing and one-to-one, and $A = 10^z$. The probability density function of z is

$$h(z) = \frac{\mathrm{d}A}{\mathrm{d}z} \cdot g(10^z) = \ln(10)10^{2z}\exp\left(-10^{2z}/2\right). \tag{C2}$$

The mean of z is given by the integral

$$\overline{z} = \int_{-\infty}^{\infty} z \cdot h(z)\mathrm{d}z = \int_{-\infty}^{\infty} z \cdot \ln(10)10^{2z}\exp\left(-10^{2z}/2\right)\mathrm{d}z. \tag{C3}$$

Let $u = 10^{2z}/2$, then $\mathrm{d}u = \ln(10)10^{2z}\,\mathrm{d}z$ and $z = \log_{10}(2u)/2$ or $z = \frac{1}{2}\ln(2u)/\ln(10)$. With this, the integral transforms into

$$\begin{aligned}\overline{z} &= \frac{1}{2\ln(10)}\int_0^{\infty} \ln(2u)e^{-u}\mathrm{d}u \\ &= \frac{1}{2\ln(10)}\int_0^{\infty} \left[\ln(2)e^{-u} + \ln(u)e^{-u}\right]\mathrm{d}u \\ &= \frac{\ln(2)-\gamma}{2\ln(10)},\end{aligned} \tag{C4}$$

where γ is Euler's constant. The centered probability distribution is then finally given by

$$f_Z(z) = \ln(10)10^{2(z-\overline{z})}\exp\left(-10^{2(z-\overline{z})}/2\right). \tag{C5}$$

Note that this distribution is independent of the underlying standard deviations of X and Y in a specific dataset, as long as z is shifted by mean(z) in the data analysis. The shifted distribution will then follow Eq. C5 with $\overline{z}$ from Eq. C4.

[1] M. Maiuri, M. Garavelli, and G. Cerullo, "Ultrafast Spectroscopy: State of the Art and Open Challenges," J. Am. Chem. Soc. **142**, 3–15 (2020).
[2] C. Thomsen, J. Strait, Z. Vardeny, H. J. Maris, J. Tauc, and J. J. Hauser, "Coherent Phonon Generation and Detection by Picosecond Light Pulses," Phys. Rev. Lett. **53**, 989–992 (1984).
[3] P. Ruello and V. E. Gusev, "Physical mechanisms of coherent acoustic phonons generation by ultrafast laser action," Ultrasonics **56**, 21–35 (2015).
[4] T. Saito, O. Matsuda, M. Tomoda, and O. B. Wright, "Imaging gigahertz surface acoustic waves through the photoelastic effect," J. Opt. Soc. Am. B **27**, 2632–2638 (2010).
[5] A. Abbas, Y. Guillet, J.-M. Rampnoux, P. Rigail, E. Mottay, B. Audoin, and S. Dilhaire, "Picosecond time resolved opto-acoustic imaging with 48 MHz frequency resolution," Opt. Express **22**, 7831–7843 (2014).
[6] F. Decremps, M. Gauthier, S. Ayrinhac, L. Bove, L. Belliard, B. Perrin, M. Morand, G. Le Marchand, F. Bergame, and J. Philippe, "Picosecond acoustics method for measuring the thermodynamical properties of solids and liquids at high pressure and high temperature," Ultrasonics **56**, 129–140 (2015).
[7] Z. Ding, K. Chen, B. Song, J. Shin, A. A. Maznev, K. A. Nelson, and G. Chen, "Observation of second sound in graphite over 200 K," Nat. Commun. **13**, 285 (2022).
[8] W. Yan, A. V. Akimov, M. Barra-Burillo, M. Bayer, J. Bradford, V. E. Gusev, L. E. Hueso, A. Kent, S. Kukhtaruk, A. Nadzeyka, A. Patanè, A. W. Rushforth, A. V. Scherbakov, D. D. Yaremkevich, and T. L. Linnik, "Coherent Phononics of van der Waals Layers on Nanogratings," Nano Lett. **22**, 6509–6515 (2022).
[9] T. Dehoux, M. A. Ghanem, O. F. Zouani, J.-M. Rampnoux, Y. Guillet, S. Dilhaire, M.-C. Durrieu, and B. Audoin, "All-optical broadband ultrasonography of single cells," Sci. Rep. **5**, 8650 (2015).
[10] B. Audoin, "Principles and advances in ultrafast photoacoustics; applications to imaging cell mechanics and to probing cell nanostructure," Photoacoustics **31**, 100496 (2023).
[11] B. C. Daly, N. C. R. Holme, T. Buma, C. Branciard, T. B. Norris, D. M. Tennant, J. A. Taylor, J. E. Bower, and S. Pau, "Imaging nanostructures with coherent phonon pulses," Appl. Phys. Lett. **84**, 5180–5182 (2004).
[12] A. Antoncecchi, H. Zhang, S. Edward, V. Verrina, P. C. M. Planken, and S. Witte, "High-resolution microscopy through optically opaque media using ultrafast photoacoustics," Opt. Express **28**, 33937–33947 (2020).
[13] S. Edward, H. Zhang, I. Setija, V. Verrina, A. Antoncecchi, S. Witte, and P. Planken, "Detection of Hidden Gratings through Multilayer Nanostructures Using Light and Sound," Phys. Rev. Appl. **14**, 014015 (2020).
[14] P. A. Elzinga, F. E. Lytle, Y. Jian, G. B. King, and N. M. Laurendeau, "Pump/Probe Spectroscopy by Asynchronous Optical Sampling," Appl. Spectrosc. **41**, 2–4 (1987).
[15] A. Bartels, A. Thoma, C. Janke, T. Dekorsy, A. Dreyhaupt, S. Winnerl, and M. Helm, "High-resolution THz spectrometer with kHz scan rates," Opt. Express **14**, 430–437 (2006).
[16] A. Bartels, R. Cerna, C. Kistner, A. Thoma, F. Hudert, C. Janke, and T. Dekorsy, "Ultrafast time-domain spectroscopy based on high-speed asynchronous optical sampling," Rev. Sci. Instrum. **78**, 035107 (2007).
[17] R. Gebs, G. Klatt, C. Janke, T. Dekorsy, and A. Bartels, "High-speed asynchronous optical sampling with sub-50fs time resolution," Opt. Express **18**, 5974–5983 (2010).
[18] G. Klatt, R. Gebs, C. Janke, T. Dekorsy, and A. Bartels, "Rapid-scanning terahertz precision spectrometer with more than 6 THz spectral coverage," Opt. Express **17**, 22847–22854 (2009).
[19] G. Klatt, R. Gebs, H. Schäfer, M. Nagel, C. Janke, A. Bartels, and T. Dekorsy, "High-Resolution Terahertz Spectrometer," IEEE J. Sel. Top. Quantum Electron. **17**, 159–168 (2011).
[20] O. Kliebisch, D. C. Heinecke, and T. Dekorsy, "Ultrafast time-domain spectroscopy system using 10 GHz asynchronous optical sampling with 100 kHz scan rate," Opt. Express **24**, 29930–29940 (2016).
[21] C. Li, N. Krauß, G. Schäfer, L. Ebner, O. Kliebisch, J. Schmidt, S. Winnerl, M. Hettich, and T. Dekorsy, "High-speed asynchronous optical sampling based on GHz Yb:KYW oscillators," Opt. Express **25**, 9204–9212 (2017).
[22] Y. Kim and D.-S. Yee, "High-speed terahertz time-domain spectroscopy based on electronically controlled optical sampling," Opt. Lett. **35**, 3715–3717 (2010).
[23] R. J. B. Dietz, N. Vieweg, T. Puppe, A. Zach, B. Globisch, T. Göbel, P. Leisching, and M. Schell, "All fiber-coupled THz-TDS system with kHz measurement rate based on electronically controlled optical sampling," Opt. Lett. **39**, 6482–6485 (2014).

[24]M. Yahyapour, A. Jahn, K. Dutzi, T. Puppe, P. Leisching, B. Schmauss, N. Vieweg, and A. Deninger, "Fastest Thickness Measurements with a Terahertz Time-Domain System Based on Electronically Controlled Optical Sampling," Appl. Sci. **9**, 1283 (2019).
[25]F. Hooge, "1/f noise sources," IEEE Trans. Electron Devices **41**, 1926–1935 (1994).
[26]M. J. Feldstein, P. Vöhringer, and N. F. Scherer, "Rapid-scan pump–probe spectroscopy with high time and wave-number resolution: Optical-Kerr-effect measurements of neat liquids," J. Opt. Soc. Am. B **12**, 1500–1510 (1995).
[27]O. Matsuda, M. C. Larciprete, R. Li Voti, and O. B. Wright, "Fundamentals of picosecond laser ultrasonics," Ultrasonics **56**, 3–20 (2015).
[28]H. Zhang, A. Antoncecchi, S. Edward, I. Setija, P. Planken, and S. Witte, "Unraveling Phononic, Optoacoustic, and Mechanical Properties of Metals with Light-Driven Hypersound," Phys. Rev. Appl. **13**, 014010 (2020).
[29]P. Welch, "The use of fast Fourier transform for the estimation of power spectra: A method based on time averaging over short, modified periodograms," IEEE Trans. Audio Electroacoust. **15**, 70–73 (1967).
[30]G. Heinzel, A. Rüdiger, and R. Schilling, "Spectrum and spectral density estimation by the Discrete Fourier transform (DFT), including a comprehensive list of window functions and some new at-top windows," Tech. Rep. (Max Planck Institute for Gravitational Physics, Hannover, 2002).
[31]B. Rivet, L. Girin, and C. Jutten, "Log-Rayleigh Distribution: A Simple and Efficient Statistical Representation of Log-Spectral Coefficients," IEEE Trans. Audio Speech Lang. Process. **15**, 796–802 (2007).
[32]F. Quinlan, T. M. Fortier, H. Jiang, and S. A. Diddams, "Analysis of shot noise in the detection of ultrashort optical pulse trains," J. Opt. Soc. Am. B **30**, 1775–1785 (2013).

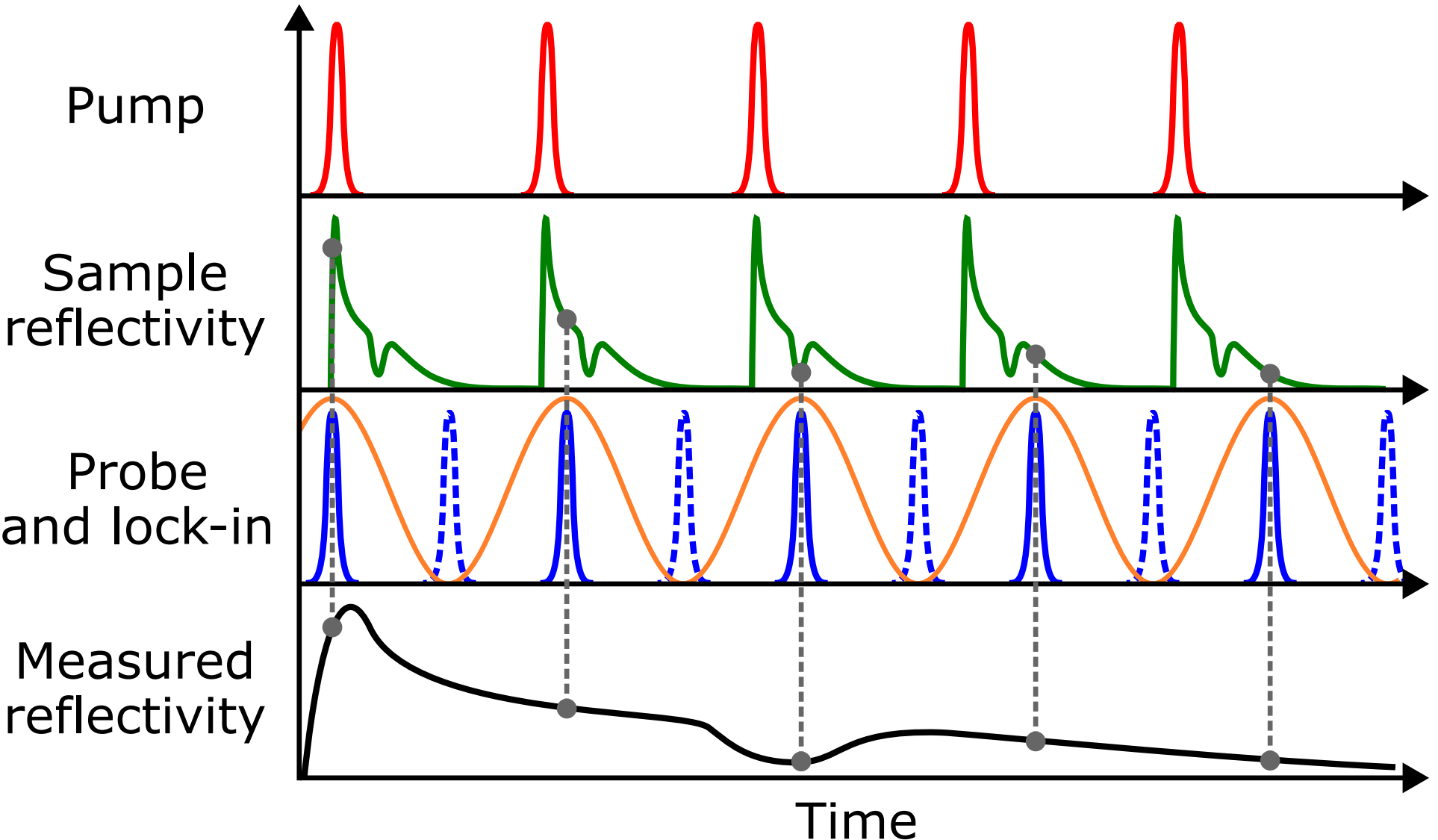
Pump
Sample reflectivity
Probe and lock-in
Measured reflectivity
Time

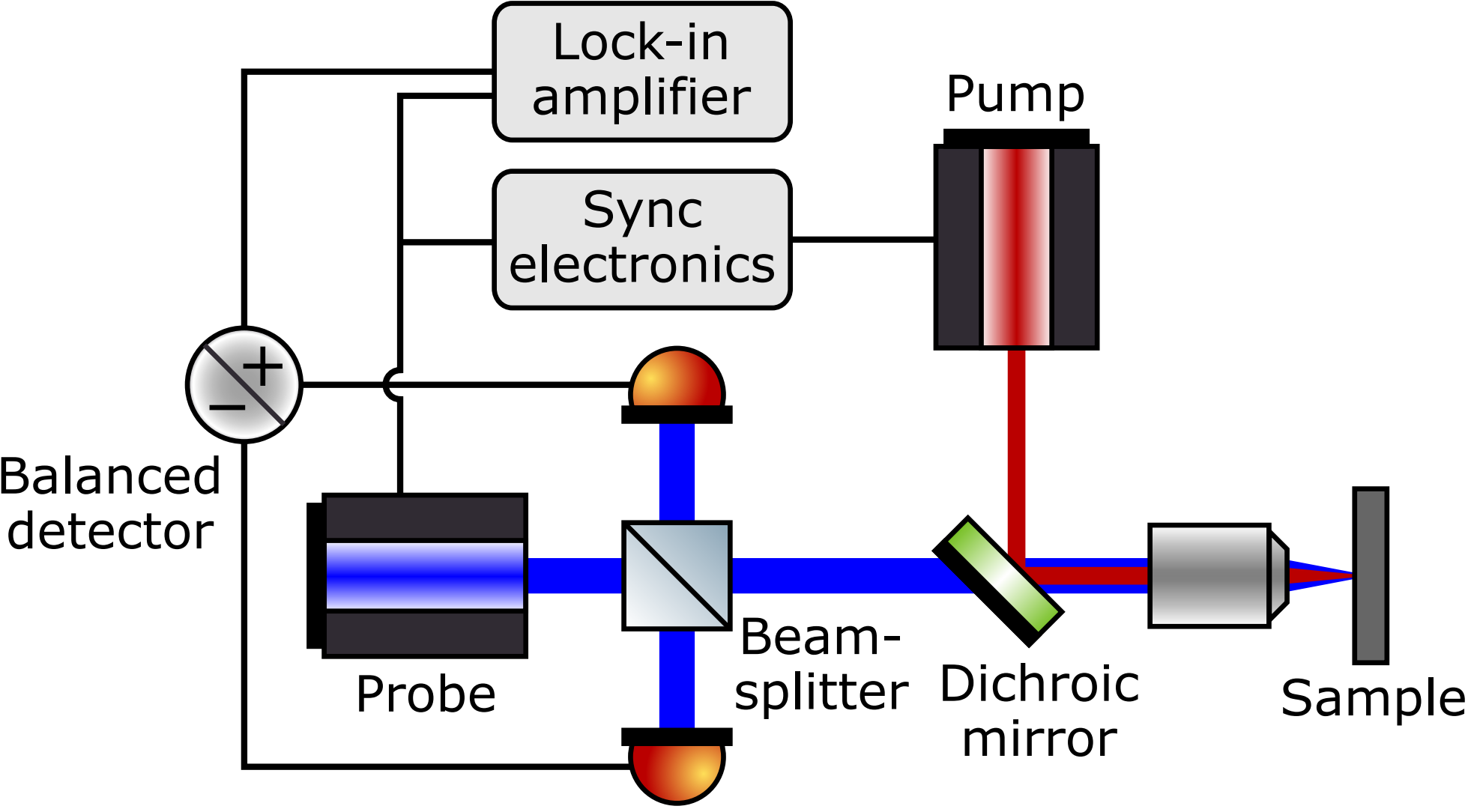
Lock-in amplifier
Sync electronics
Pump
Balanced detector
Probe
Beam-splitter
Dichroic mirror
Sample

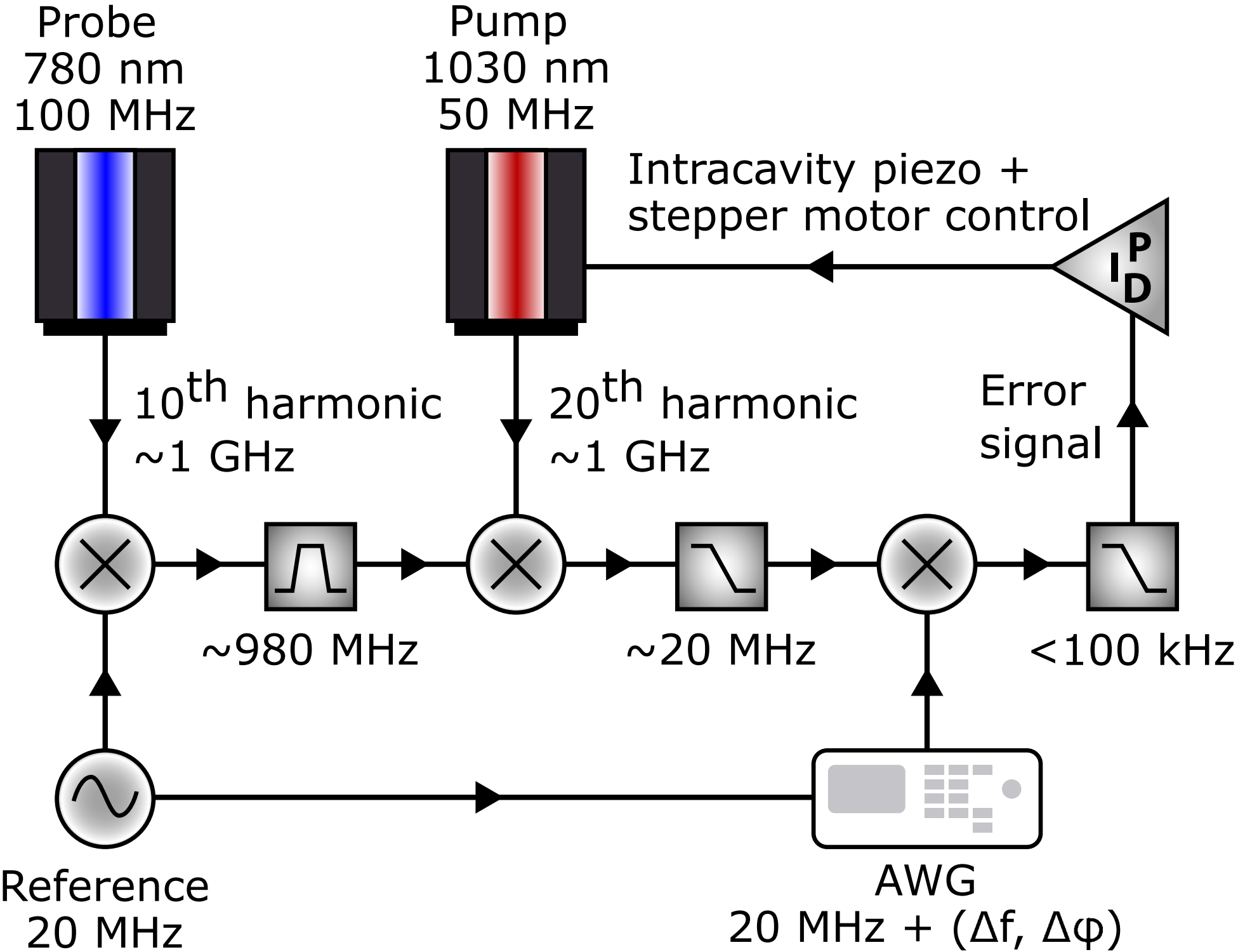
Probe
780 nm
100 MHz
Pump
1030 nm
50 MHz
Intracavity piezo +
stepper motor control
P
I
D
10th harmonic
~1 GHz
20th harmonic
~1 GHz
Error
signal
~980 MHz
~20 MHz
<100 kHz
Reference
20 MHz
AWG
20 MHz + (Δf, Δφ)

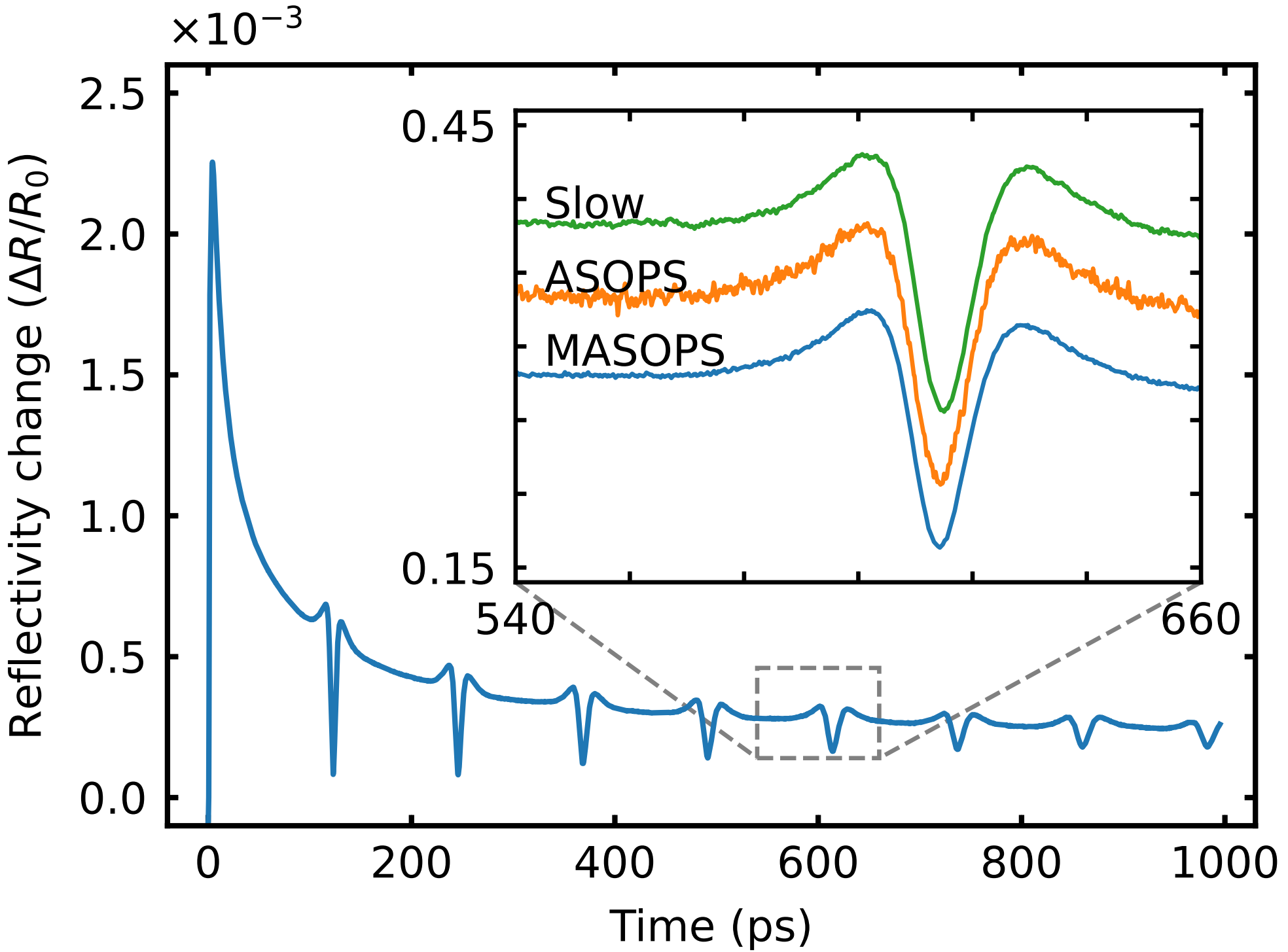
×10⁻³
2.5
2.0
1.5
1.0
0.5
0.0
Reflectivity change (ΔR/R₀)
0
200
400
600
800
1000
Time (ps)
0.45
0.15
540
660
Slow
ASOPS
MASOPS

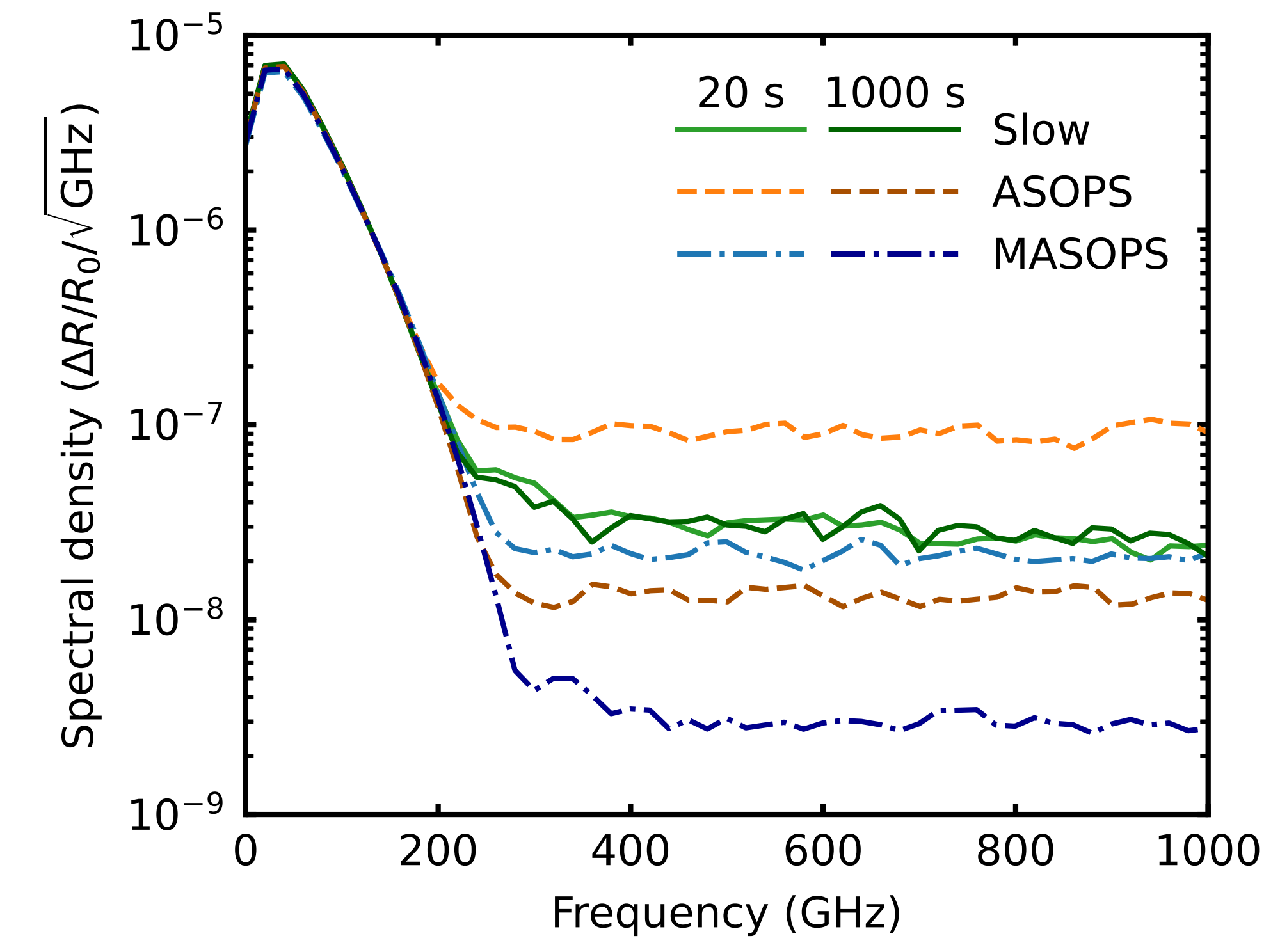
20 s
1000 s
Slow
ASOPS
MASOPS
10^{-5}
10^{-6}
10^{-7}
10^{-8}
10^{-9}
Spectral density ($\Delta R/R_0/\sqrt{\text{GHz}}$)
0
200
400
600
800
1000
Frequency (GHz)

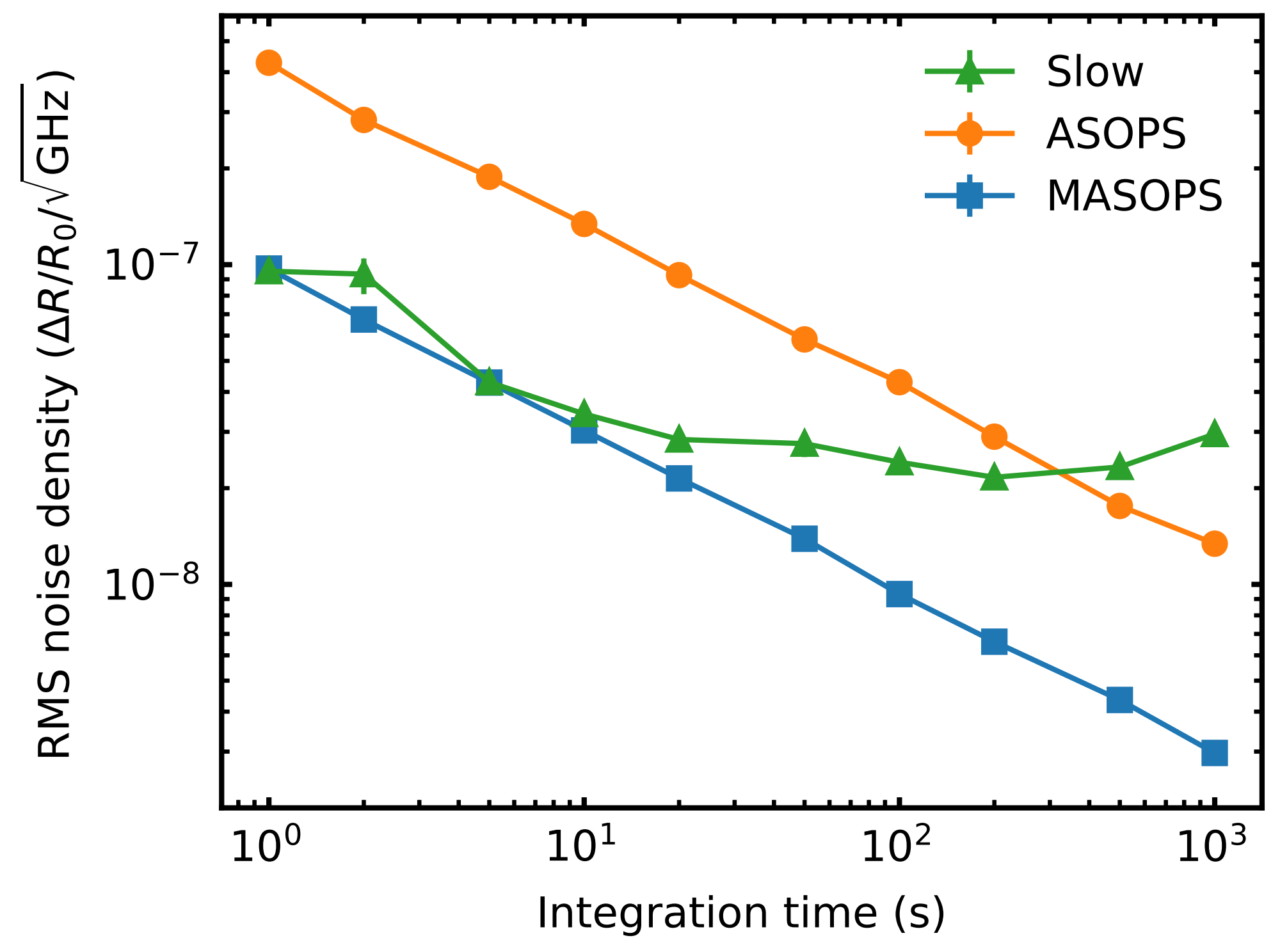
Slow
ASOPS
MASOPS
RMS noise density ($\Delta R/R_0/\sqrt{\text{GHz}}$)
10^{-7}
10^{-8}
10^0
10^1
10^2
10^3
Integration time (s)

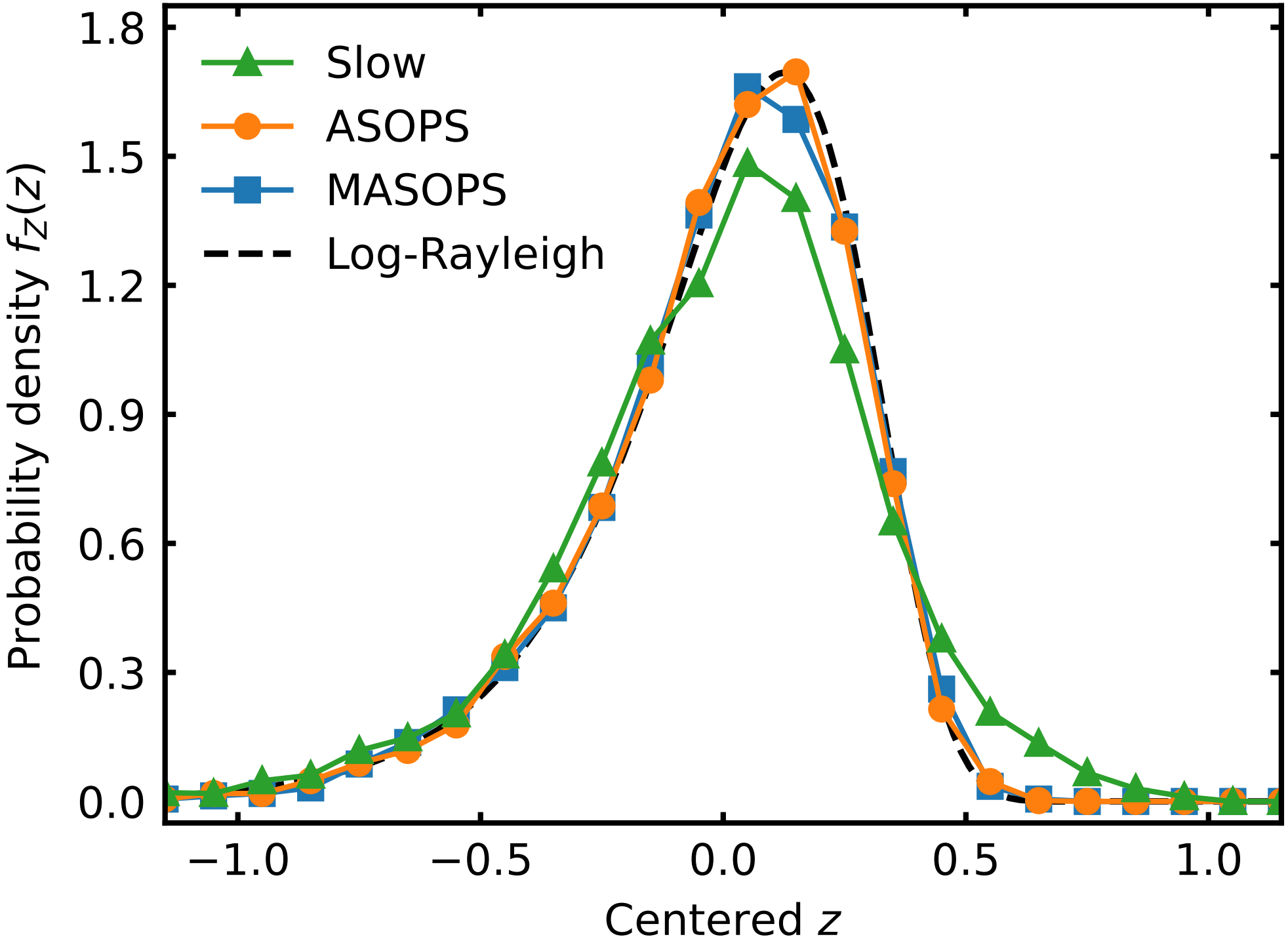
Slow
ASOPS
MASOPS
Log-Rayleigh
Probability density $f_Z(z)$
Centered z
1.8
1.5
1.2
0.9
0.6
0.3
0.0
−1.0
−0.5
0.0
0.5
1.0

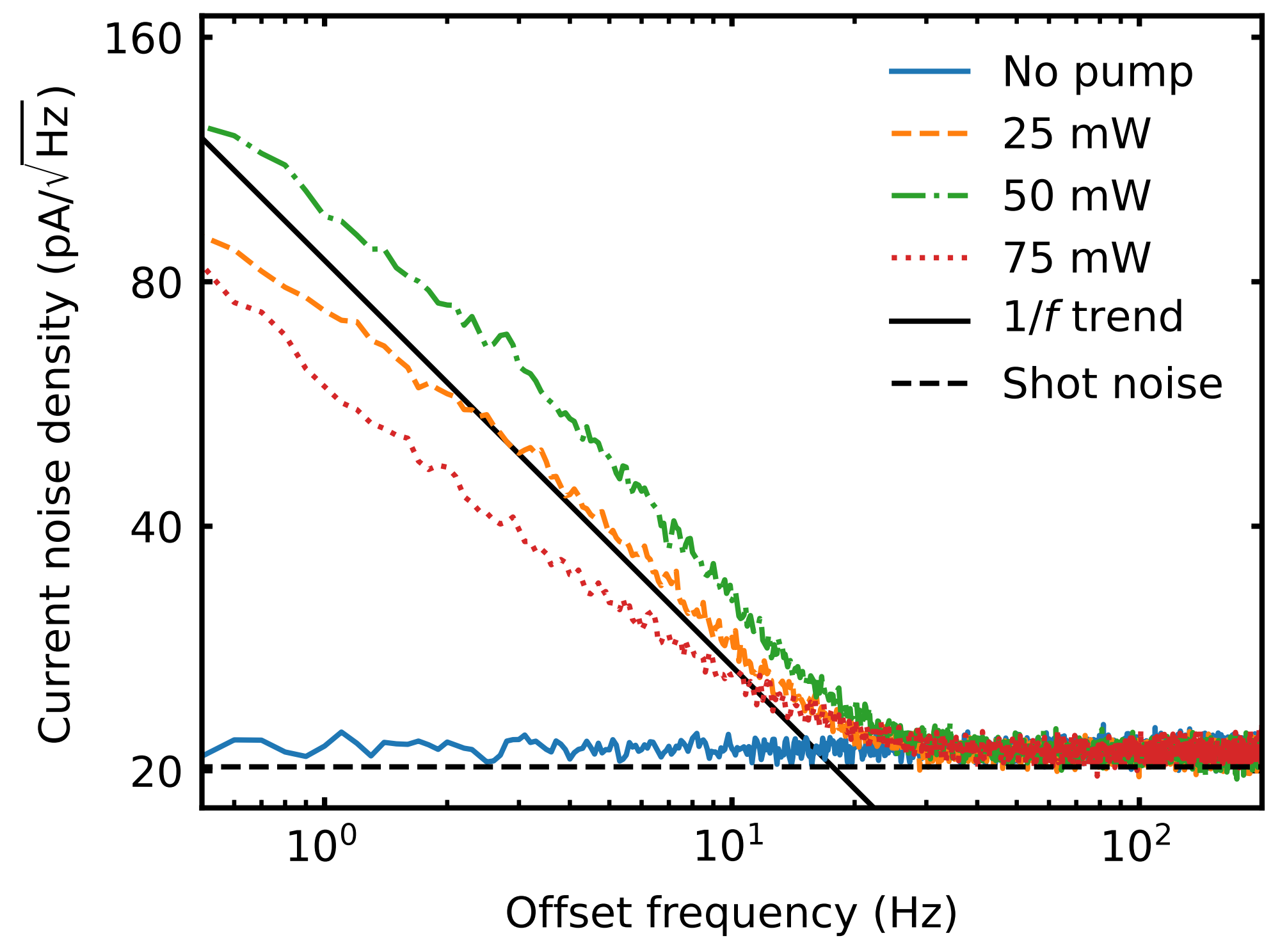
160
80
40
20
Current noise density (pA/√Hz)
10^0
10^1
10^2
Offset frequency (Hz)
No pump
25 mW
50 mW
75 mW
1/f trend
Shot noise